From particles to orbits: precise dark matter density profiles using dynamical information

Claudia Muni [⊙],[1][★] Andrew Pontzen,[1] Jason L. Sanders [⊙],[1] Martin P. Rey [⊙],[2] Justin I. Read [⊙][3] and Oscar Agertz [⊙][4]

[1]*Department of Physics & Astronomy, University College London, Gower Street, London WC1E 6BT, UK*
[2]*Sub-department of Astrophysics, University of Oxford, DWB, Keble Road, Oxford OX1 3RH, UK*
[3]*School of Mathematics & Physics, University of Surrey, Guildford GU2 7XH, UK*
[4]*Lund Observatory, Division of Astrophysics, Department of Physics, Lund University, Box 43, SE-221 00 Lund, Sweden*

ABSTRACT
We introduce a new method to calculate dark matter halo density profiles from simulations. Each particle is 'smeared' over its orbit to obtain a dynamical profile that is averaged over a dynamical time, in contrast to the traditional approach of binning particles based on their instantaneous positions. The dynamical and binned profiles are in good agreement, with the dynamical approach showing a significant reduction in Poisson noise in the innermost regions. We find that the inner cusps of the new dynamical profiles continue inward all the way to the softening radius, reproducing the central density profile of higher resolution simulations within the 95 per cent confidence intervals, for haloes in virial equilibrium. Folding in dynamical information thus provides a new approach to improve the precision of dark matter density profiles at small radii, for minimal computational cost. Our technique makes two key assumptions that the halo is in equilibrium (phase mixed) and the potential is spherically symmetric. We discuss why the method is successful despite strong violations of spherical symmetry in the centres of haloes, and explore how substructures disturb equilibrium at large radii.

Key words: galaxies: haloes – galaxies: kinematics and dynamics – dark matter.

1 INTRODUCTION

The observationally inferred density distribution of dark matter in haloes around galaxies offers a crucial hint as to the nature of the elusive substance. However, the observations must be carefully compared with theoretical predictions based largely on numerical simulations (for reviews, see e.g. Frenk & White 2012; Vogelsberger et al. 2020; Angulo & Hahn 2022). Dark-matter-only (DMO) simulations have shown that the spherically averaged density profiles of haloes in the cold dark matter (CDM) paradigm follow approximately the Navarro–Frenk–White (NFW) profile (Dubinski & Carlberg 1991; Navarro, Frenk & White 1996b, 1997; Dutton & Macciò 2014) described by a divergent cusp ($\rho \sim r^{-1}$) at small radii, and by a steeper power law ($\rho \sim r^{-3}$) in the outer regions. The NFW profile has two free parameters that may be fitted to the density structure of simulated haloes for most of the radial extent, but the fit becomes poor in the innermost parts and in the outskirts of the haloes (e.g. Navarro et al. 2004; Diemer & Kravtsov 2014; Fielder et al. 2020; Wang et al. 2020; Lucie-Smith et al. 2022).

Over time, a variety of fitting functions have been proposed to better represent the profile's inner slope, such as Einasto models (Einasto 1965; Chemin, de Blok & Mamon 2011) or other forms of double power law (e.g. Hernquist 1990; Burkert 1995; Zhao

1996; Salucci et al. 2007; Hague & Wilkinson 2013; Oldham & Auger 2016; Hayashi, Chiba & Ishiyama 2020). However, the central regions of the profiles remain notoriously difficult to probe due to the finite number of particles and consequent need to 'soften' the potential (e.g. Power et al. 2003; Diemand, Moore & Stadel 2004; Dehnen & Read 2011), causing the cusp to be numerically flattened (e.g. Navarro, Frenk & White 1996b; Ghigna et al. 2000; Fukushige & Makino 2001; Wang et al. 2020). Constraining the central asymptotic behaviour of the profile therefore remains largely dependent on the number of particles concentrated at small radii.

While the focus in this work will be on DMO simulations, we note that when baryons are added into simulations, effects such as supernova feedback and enhanced dynamical friction can cause the central cusp to turn into a flattened density 'core' (e.g. Navarro, Eke & Frenk 1996a; El-Zant, Shlosman & Hoffman 2001; Read & Gilmore 2005; Pontzen & Governato 2012; Nipoti & Binney 2014; Popolo & Pace 2016; Read, Agertz & Collins 2016; Orkney et al. 2022). Ultimately, understanding the predicted distribution of dark matter does require such baryonic simulations, especially since there are strong indications of flattened central cores in observations (see e.g. Flores & Primack 1994; de Blok, McGaugh & Rubin 2001; Marchesini et al. 2002; Battaglia et al. 2008; Walker & Peñarrubia 2011; Oh et al. 2015; Read et al. 2017; Read, Walker & Steger 2019; Zoutendijk et al. 2021; De Leo et al. 2023; or for countering views, see Pineda et al. 2016; Genina et al. 2017; Oman et al. 2018). The focus in this work is none the less on understanding how DMO

[★] E-mail: claudia.muni.21@ucl.ac.uk

predictions can be improved and better understood; we will consider baryonic effects in a future paper.

In the outskirts of haloes, density profiles scatter significantly due to the presence of surrounding substructures and the out-of-equilibrium dynamics of accreting material. For instance, the caustics generated by the infalling particles on their first apocentre passage set the scale for the splashback radius, which creates an observable signature in the outer regions of halo profiles (Adhikari, Dalal & Chamberlain 2014; Diemer & Kravtsov 2014; More, Diemer & Kravtsov 2015; Shin et al. 2019). Recently, Lucie-Smith et al. (2022) showed that a good fit to the diversity of halo profiles out to two virial radii can be obtained using only three free parameters (i.e. one additional parameter is sufficient to capture the diversity of these outer regions). This relatively simple behaviour may be linked to the typical orbits on which material accretes into a halo, further motivating a study of how the instantaneous profile relates to a dynamically generated equilibrium profile (e.g. Diemer 2022a, b; Shin & Diemer 2023).

In this work, we present and study a method to calculate dark matter density profiles from simulated haloes using dynamical information. This possibility has been discussed before – notably in appendices to Read & Gilmore (2005) and Pontzen & Governato (2013), and in Callingham et al. (2020) – but its possible application to reducing the noise in numerical density estimates has not been explored in detail. Specifically, the technique 'smears' particles in a snapshot along their orbits, spreading the mass of each across multiple density bins. Such a dynamical approach shares some similarities with certain classical mass modelling techniques (Schwarzschild 1979; Syer & Tremaine 1996) but, unlike these, it does not attempt to match observational constraints to underlying orbits and potentials; rather, it constructs these from a simulation snapshot. The result is a profile that is averaged over a dynamical time, and that consequently has reduced Poisson noise compared to traditional binned estimates at the same resolution. This, in turn, makes it possible to probe further into the behaviour of the inner regions, at radii where there are very few particles present.

Calculating a density profile through this averaging process inherently assumes an equilibrium, phase-mixed distribution function. This assumption is expected to be significantly broken in the outer parts of a halo approaching the virial radius or beyond. Furthermore, for a practical calculation, we will also assume spherical symmetry (although this assumption could in principle be relaxed). The gravitational potentials of real and simulated haloes are far from being perfectly spherical. Their shapes tend to be closer to triaxial, especially towards the centre (e.g. Frenk et al. 1988; Jing & Suto 2002; Allgood et al. 2006; Orkney et al. 2023); however, it has previously been argued using Hamiltonian perturbation theory that approximating the true triaxial potential by a spherically averaged version should make little difference to dynamical density estimates if the system is in equilibrium (Pontzen et al. 2015). We will return to this point in our discussion. Our results focus on the innermost and the outermost regions of haloes to investigate the limits of dynamical halo profiles subject to these coupled assumptions of equilibrium and spherical symmetry.

The rest of the paper is structured as follows. In Section 2, we explain the procedure used to generate the dynamical density profiles. In Section 3, we describe the simulation suites and the selection of snapshots analysed in this work. In Section 4, we present the main results for the dynamical profiles, focusing on the inner and outer regions, and comparing our dynamical technique to traditional binned methods. In Section 5, we discuss the implication of our results and outline possible further work.

2 METHODS

We now describe the methods used to construct dynamical profiles. Section 2.1 considers the construction of a spherically averaged gravitational potential starting from a simulation snapshot, the calculation of particle orbits within that potential, and finally the computation of the dynamical density profile. In Section 2.2, we introduce a refinement to the method that improves the accuracy of the orbit integration around apocentre and pericentre. Then, in Section 2.3, we describe an iterative process via which a self-consistent density–potential pair may be generated.

2.1 Creating the dynamical density profiles

We start by assuming that we have a snapshot containing only dark matter particles, centred on the target halo. The spherically averaged gravitational potential given by all the particles in the snapshot is then calculated in bins of width Δr according to the discretized integral

$$\Phi(r_k) = G \sum_{j=1}^{k} \frac{M(<r_j)}{r_j^2} \Delta r, \tag{1}$$

where j is an index over the bins, k is the bin number for which the potential is being calculated, and r_j is the radius in the centre of the jth bin, taking the value $r_j = (j - 1/2)\Delta r$. In addition, $M(<r_j)$ is the mass enclosed within radius r_j, and G is the gravitational constant. Although the potential for each bin k is evaluated from quantities at the centre of the bin, the values are assigned to the right edge of the corresponding bins, since $\Phi(r_k)$ represents the average of the potential over the entire bin k. The zero point of the potential is set at $r = 0$ (the left edge of the first bin). Equation (1) is the simplest of several possible choices to perform numerical integration. We tested that adopting a more sophisticated method does not significantly affect the final results. Therefore, we adopted the simple approach for transparency.

The total number of bins over which Φ is calculated is determined by the radius of a 'bounding sphere' centred around the halo. In addition to choosing the radius at which to truncate the potential, we must also decide how to treat particles whose orbits cross this boundary. In keeping with the core assumption of equilibrium, we make the boundary *reflecting*, i.e. particles bounce elastically off it. One may equivalently imagine the potential as having an infinite potential step at the truncation radius. While this is unphysical for any individual particle considered in isolation, across the population it is equivalent to the much more reasonable assumption that the outwards flux through the sphere is balanced by a matching inwards flux. This assumption can be tested by changing the truncation radius; the halo virial radius is a natural first choice, and we will explore the effects of other choices on the final density profile in Section 4.2.2.

Assuming equilibrium, the probability density $p_i(r)$ of finding particle i at radius r is proportional to the time spent by the particle in the infinitesimal interval around that radius:

$$p_i(r) = \frac{1}{T_i} \int_0^{T_i} \delta(r - r_i(t)) \, \mathrm{d}t = \frac{2}{T_i} \frac{1}{\dot{r}(r, E_i, j_i, \Phi)}, \tag{2}$$

where $r_i(t)$ describes the radius as a function of time for the particle (on its spherical idealized orbit), T_i is the period of the orbit, E_i is its specific energy, and j_i is its specific angular momentum. Rather than calculate T_i directly we first calculate an unnormalized version of the probability, $q_{i,k} \equiv (T_i/2)p_i(r_k)$. Here, i indexes the particles, and k indexes the spatial bins. By writing the specific energy of a particle as the sum of the potential energy, the kinetic energy due to the angular momentum, and the kinetic energy due to the radial

motion, we can solve for $\dot{r}$ and obtain

$$q_{i,k} \equiv \frac{1}{\dot{r}(r_k, E_i, j_i, \Phi)} = \left(E_i - \frac{j_i^2}{2r_k^2} - \Phi(r_k) \right)^{-\frac{1}{2}}. \qquad (3)$$

Note that this expression is only valid between pericentre and apocentre; outside this radial range, it becomes imaginary. However the true probability of finding the particle outside the extrema of its orbit is zero by definition, and therefore one may make equation (3) true for all radial bins by taking its real part. We produce a normalized probability for each bin k and particle i according to

$$p_{i,k} \equiv \left(\frac{\mathfrak{Re}\, q_{i,k}}{\mathfrak{Re}\, \sum_j q_{i,j}} \right), \qquad (4)$$

where $\mathfrak{Re}$ denotes the real part. If a particle i is on an almost perfectly circular trajectory, it may remain within a single radial bin k for its entire orbit; in this case, the equation above fails and instead a unit probability is assigned to the bin enclosing the original position of the particle in the snapshot, $p_{i,k} = 1$.

The density at the centre of bin k can then be estimated from the set of $p_{i,k}$ as

$$\rho(r_k) = \frac{3}{4\pi} \sum_{i=1}^{N} \frac{m_i\, p_{i,k}}{(r_k + \Delta r/2)^3 - (r_k - \Delta r/2)^3}, \qquad (5)$$

where m_i is the mass of each particle i, and there are N particles in total.

The statistical errors in the dynamical density profile are estimated using bootstrapping. For each of 100 bootstrap samples, we create a mock set of particles by sampling (with replacement) from the actual set of particles in the halo; we then perform the full dynamical density estimate on the mock set of particles. We determined that 100 bootstrap samples was sufficient to achieve convergence on the 95 per cent confidence interval; in Section 4, our results are shown with these uncertainties as a shaded band.

2.2 Improving accuracy at apocentre and pericentre

The function in equation (3) has two integrable divergences located at the pericentre and apocentre of each orbit (Fig. 1). Unless the bins are infinitesimally small, the probability of finding the particle in the bin $p_{i,k}$ containing such a divergence might be misestimated. To correct for this, in these two bins we use an approximation scheme based on a local Taylor expansion of the potential. We define the effective potential as $\Phi_{\rm eff} = \Phi + j^2/(2r^2)$, and expand $\Phi_{\rm eff}(r_0 + \delta r)$ around r_0, where r_0 is the divergence point (pericentre or apocentre) for every orbit, i.e. a root of equation (3). We now consider the case of a pericentre where the divergence r_0 is inside the kth bin [i.e. $(k - 1)\Delta r < r_0 < k\Delta r$], as an example. The mean value of $\mathfrak{Re}\,\dot{r}^{-1}$ across the entire bin may be calculated as

$$\bar{q} \equiv \frac{1}{\Delta r} \int_{r_0}^{r_k} (E_i - \Phi_{\rm eff}(r))^{-1/2} {\rm d}r,$$

$$\approx \frac{1}{\Delta r} \int_{r_0}^{r_k} \left(-\frac{{\rm d}\Phi_{\rm eff}}{{\rm d}r} \bigg|_{r_0} (r - r_0) \right)^{-1/2} {\rm d}r. \qquad (6)$$

Here, we have also used the fact that $\Phi_{\rm eff}(r_0) = E_i$, by definition. We can furthermore approximate ${\rm d}\Phi_{\rm eff}/{\rm d}r|_{r_0} \approx {\rm d}\Phi_{\rm eff}/{\rm d}r|_{r_k}$ to avoid having to calculate the exact location of the divergences; this will give us a correction that is accurate to first order. The integration is then analytically tractable, giving

$$\bar{q} \approx \frac{1}{\Delta r} \frac{2(E_i - \Phi_{\rm eff}(r_k))^{1/2}}{{\rm d}\Phi_{\rm eff}(r_k)/{\rm d}r|_{r_k}}. \qquad (7)$$
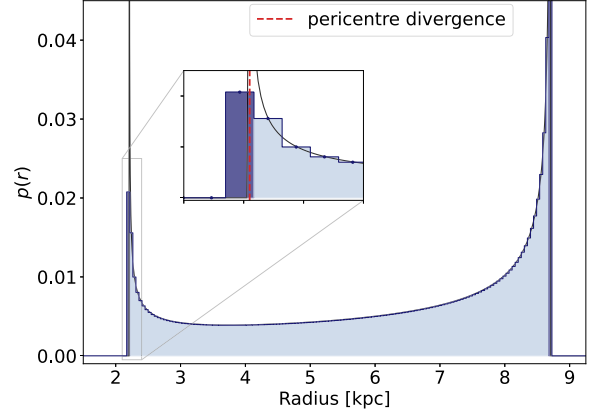
Figure 1. The binned probability density implied by equation (3) evaluated for a typical particle (light shaded bins), with a bin size $\Delta r = \epsilon/2$, compared with the analytical integrand (solid line). The integrand is well behaved for most of the radial range of the orbit, and therefore well approximated by the binned density. However, it has two integrable divergences at pericentre and apocentre (here located at $\sim$2.2 and $\sim$8.7 kpc, respectively). Even if the particle never reaches the centre of one of these extremal bins, it may still spend significant time within the bin. Capturing this effect correctly in the binned probability requires the special treatment explained in the text. The dark shaded bins represent the analytical corrections added at the pericentre and apocentre for this orbit.

This analytical estimate of the mean value is then used to represent the value of the probability density function within the pericentre bin q_k. The apocentre bin is treated in the same way, and both corrections are included before producing the normalized probability according to equation (4).

There are two cases in which these corrections cannot be evaluated. One of them is when an orbit is unresolved (i.e. its probability function only spans one bin), since in that case pericentre and apocentre are coincident. As previously stated, when this occurs, the particle is given unit probability to be found within the single bin, and corrections are not required. The apocentre corrections are also ignored when the particle's apocentre falls outside of the radius of the 'reflecting wall' that serves as the boundary for the halo. Since the particles can be thought of as being reflected back once they hit the boundary, their radial paths are truncated at the location of the wall, and no apocentre corrections are required.

2.3 Iterating the potential

The dynamical density profile given by equation (5) implies also a mass profile $M\,(<r)$ and therefore a potential $\Phi(r)$ through equation (1). However, the potential used in producing the density estimate was initialized directly using the particle radii from the original snapshot. The overall procedure therefore results in an inconsistent potential–density pair. The difference between the mass distribution is especially evident in the inner regions because our potential is calculated without softening, and the pericentres of orbits can therefore reach radii closer to the centre of the haloes. To resolve this discrepancy, we iterate until a self-consistent density-potential configuration pair is reached. Over the course of the iterations, the gravitational potential from the simulation is gradually transformed into the potential inferred from the dynamical density profile. This technique also removes any discontinuities in the derivatives of the potential at small radii due to the finite particle number.

Table 1. Properties (softening length, particle mass, number of particles, virial radius, virial mass, and brief comments on the density structure) of the seven haloes investigated in this work. The haloes can be grouped into three main categories based on their virial mass, from dwarf to Milky Way mass. The number of particles refers to the particles enclosed by each halo's virial radius at $z = 0$.

Halo	Figure	Resolution	ϵ (kpc)	Particle mass ($M_\odot$)	Number of particles	$r_{\rm vir}$ (kpc)	Virial mass ($M_\odot$)	Structure
1445	2, top	Low	0.095	7.1×10^4	3×10^4	41.7	2×10^9	Substructures at large r; dynamical equilibrium
		High	0.012	1.1×10^3	2×10^6	41.5		
1459	2, bottom	Low	0.095	7.1×10^4	3×10^4	41.4	2×10^9	Substructures at large r; dynamical equilibrium
		High	0.012	1.1×10^3	2×10^6	41.1		
		Ultra-high	0.006	1.4×10^2	1×10^7	41.1		
600	3, top	Low	0.095	7.1×10^4	8×10^4	56.8	5×10^9	Low res: recent merger, disequilibrium (cusp). Higher res: equilibrium
		High	0.012	1.1×10^3	5×10^6	56.2		
		Ultra-high	0.006	1.4×10^2	4×10^7	56.2		
605	3, middle	Low	0.095	7.1×10^4	7×10^4	55.0	5×10^9	Minimal substructure; dynamical equilibrium
		High	0.012	1.1×10^3	4×10^6	54.7		
624	3, bottom	Low	0.095	7.1×10^4	7×10^4	56.3	5×10^9	Pre-merger; significant disequilibrium
		High	0.012	1.1×10^3	5×10^6	56.2		
685	4, top	Low	0.142	2.3×10^5	5×10^6	349.0	1×10^{12}	Minimal substructure; dynamical equilibrium
		High	0.035	2.9×10^4	4×10^7	346.9		
715	4, bottom	Low	0.142	2.3×10^5	6×10^6	358.4	1×10^{12}	Minimal substructure; dynamical equilibrium
		High	0.035	2.9×10^4	5×10^7	357.3		

The iteration process involves a series of steps:

(i) A dynamical density profile is first obtained as described in Sections 2.1 and 2.2.

(ii) The mass distribution implied by the dynamical profile is calculated according to

$$M(< r_j + \Delta r/2) = \sum_{i=1}^{N} \sum_{k=1}^{j} m_i \, p_{i,k}. \tag{8}$$

The mass at the centre of the bin (r_j) is then obtained by averaging the mass at adjacent edges.

(iii) The new mass distribution is inserted into equation (1) to evaluate a new gravitational potential.

(iv) The angular momenta of the particles is assumed to be unchanged, and the energies are updated by keeping the radial action constant at first order (see below).

(v) The cycle is repeated, starting from point (ii) and using the updated dynamical profile, until convergence in the dynamical profile is reached.

Evolving the gravitational potential into the new configuration will affect the phase space distribution of the particles. Hence, we require the energies of the particles to change accordingly. In step (iv), the updated energies are calculated by keeping the radial action of each particle constant to first order,

$$J_r(E_{{\rm new},i}, j_i, \Phi_{\rm new}) = J_r(E_{{\rm old},i}, j_i, \Phi_{\rm old}) + \mathcal{O}(\Delta \Phi^2), \tag{9}$$

for each particle i, where $E_{{\rm new},i}$, $\Phi_{\rm new}$ and $E_{{\rm old},i}$, $\Phi_{\rm old}$ are the specific energy and the potential after and before the iteration respectively, and $\Delta \Phi = \Phi_{\rm new} - \Phi_{\rm old}$. We keep J_r constant since we can interpret each iteration as a small change to the potential of the halo, akin to an adiabatic relaxation. This process does not correspond to a literal physical evolution of the halo in time, but an adiabatic transformation is none the less the most conservative way to map orbits from the potential at each iteration to the next. In other words, we assume that the action distribution of the particles in the simulation is sampled from an underlying 'true' distribution (as would be attained by a simulation of infinite resolution). We then recover the potential implied by the dynamical profile given this action distribution. If we assume that the change to the potential between iterations is sufficiently small, we only need update the actions at first order in the potential change, i.e. equation (9).

The definition of the radial action is

$$J_r(E, j, \Phi) = \frac{2}{\pi} \int_{r_{\rm peri}}^{r_{\rm apo}} \sqrt{E - \frac{j^2}{2r^2} - \Phi(r)} \, dr \,. \tag{10}$$

With this in hand, we solve equation (9) to first order in the quantities $\Delta \Phi$ and $\Delta E_i = E_{{\rm new},i} - E_{{\rm old},i}$. By Taylor expanding, we find

$$\Delta E_i \approx \frac{\int_{r_{\rm peri}}^{r_{\rm apo}} \Delta \Phi(r) \left(E_{{\rm old},i} - \frac{j_i^2}{2r^2} - \Phi_{\rm old}(r)\right)^{-1/2} dr}{\int_{r_{\rm peri}}^{r_{\rm apo}} \left(E_{{\rm old},i} - \frac{j_i^2}{2r^2} - \Phi_{\rm old}(r)\right)^{-1/2} dr} = \langle \Delta \Phi \rangle, \tag{11}$$

i.e. the change in energy is equal to the average of the change in potential, weighted by the probability of finding the particle at a given radius. (At first order, the changes to the values of apocentre and pericentre of the orbit do not contribute to ΔE, and can therefore be neglected.)

The first iteration produces a significant change in the inner density distribution but after approximately three iterations, convergence in the dynamical profile is reached (i.e. the changes in the density profiles become significantly smaller than the bootstrap-determined uncertainties). We will discuss this further in Section 4.1.2.

3 THE SIMULATION SNAPSHOTS

We analyse a selection of seven snapshots drawn from cosmological zoom simulations of dark matter haloes spanning a wide range of masses, from $\sim 10^9$ to $\sim 10^{12} \, M_\odot$ (see Table 1).

The five smallest haloes are part of the Engineering Dwarfs at Galaxy Formation's Edge (EDGE) project (Agertz et al. 2019; Rey et al. 2019, 2020; Orkney et al. 2021); the two largest haloes were taken from the VINTERGATAN-GM project, which in turn uses the initial conditions described by Rey & Starkenburg (2021). Both suites of simulations assume a ΛCDM cosmology: EDGE adopts

cosmological parameters based on data from Planck Collaboration XVI ([2014]) ($\Omega_m = 0.309$, $\Omega_\Lambda = 0.691$, $H_0 = 67.77$ km s^{-1} Mpc^{-1}) with a box size of 50 Mpc, while VINTERGATAN-GM uses cosmological parameters from Planck Collaboration XIII ([2016]) ($\Omega_m = 0.314$, $\Omega_\Lambda = 0.686$, $H_0 = 67.27$ km s^{-1} Mpc^{-1}) with a box size of 73 Mpc. As previously stated, we consider the DMO simulations from these suites, i.e. they do not contain any baryonic components; hence, steep cusps are expected in the central regions of the density profiles.

The selected haloes were re-simulated at two different resolutions; the particle mass ratio between the lower and in the higher resolution runs is 64 (for EDGE) and 8 (for VINTERGATAN-GM). Both suites of simulations are generated using the adaptive mesh refinement (AMR) code RAMSES (Teyssier [2002]). The mesh is refined whenever a grid cell contains more than eight particles; consequently, the softening lengths are adaptive and we provide a softening scale estimate ϵ equal to the size of the smallest grid cell used for gravity calculations. We call *low resolution* the simulations with softening scale of 0.095 kpc (0.142 kpc for the VINTERGATAN-GM haloes), and *high resolution* the ones with softening of 0.012 kpc (0.035 kpc for the VINTERGATAN-GM haloes). *Ultra-high-resolution* runs with softening scale ~0.006 kpc are also available for some EDGE simulations. All the snapshots analysed in the current work are taken at the present day ($z = 0$).

Simulation snapshots are loaded using pynbody (Pontzen et al. [2013]). Before processing, each halo is centred using the shrinking-sphere method of Power et al. ([2003]); the central 1 kpc is used to calculate a centre of mass velocity, which is then subtracted from all particles. We also calculate a virial radius, r_{vir}, defined to be the radius at which the enclosed mean density is equal to 178 times the cosmic mean.

All particles interior to the reflecting wall at the time of the snapshot are included in the calculations. Some of the selected haloes contain large substructures, especially in their outskirts; these are deliberately retained in our analysis in order to test the limits of the assumption of equilibrium. The reflecting boundary described in Section [2.1] was placed at 120 kpc for the haloes with mass $\lesssim 5 \times 10^9$ M$_\odot$. This is between two and three times the size of their virial radii, a choice that allows us to explore how the dynamical information affects the density distribution in their outer regions. The boundary for the two largest haloes was placed at 350 kpc, which is approximately the location of their virial radii, and was not extended to larger radii in this work because the 'zoomed' region of these haloes is only twice the virial radius, beyond which low-resolution particles are present. For efficiency, the dynamical profiles of the two largest haloes are generated using only a randomly selected fraction (a third) of the particles.

While it is not possible to recreate precisely the in-simulation softening ϵ with a spherical approximation, it is clear that the bin width Δr must be comparable to ϵ in order that the potential is meaningful. We found that our results were insensitive to the precise bin width chosen, provided that it is of this order, and therefore chose to fix $\Delta r = \epsilon/2$. This choice of bin width is sufficiently small to allow investigation of the dynamically inferred density profile close to the halo centre. We note that for $r \lesssim 3\epsilon \equiv r_{conv}$ the effect of spurious relaxation in simulation becomes important and a profile constructed through direct particle binning is poorly resolved. Detailed studies of convergence (e.g. Power et al. [2003]; Gao et al. [2012]; Ludlow, Schaye & Bower [2019]) show that the value of r_{conv} must be determined empirically for each simulation set-up, and any relation to the softening length ϵ is approximate; the scale is mainly dictated by the number of particles present in the innermost regions.

Our comparisons of binned profiles between high- and low-resolution simulations below confirm that $r_{conv} \sim 3\epsilon$ gives a sufficiently good approximation to the innermost reliable radius of the low-resolution binned profiles.[1]

4 RESULTS

In this section, we present and discuss the dynamical density profiles of our dark matter haloes. In each case, we calculate dynamical profiles from the low-resolution snapshots and compare them with binned profiles from both low- and high-resolution snapshots. The profiles are shown in Figs [2]–[4] (for lowest mass dwarf, intermediate-mass dwarf, and Milky Way-mass haloes, respectively), alongside images of the haloes' dark matter density projected down the z-axis. We compare our dynamical profiles (blue lines) to the traditional binned estimates from both the high and the low-resolution snapshots (black and pink points, respectively), which are plotted down to their estimated softening length (see Table [1]). Inset panels show the inner density profile in greater detail.

Overall, the dynamical profiles (blue lines), obtained from the low-resolution simulations, agree well with the low-resolution binned profiles (pink points) for the majority of the radial extent of the haloes. The 95 per cent bootstrap-determined uncertainties on the dynamical profiles are shown as shaded blue bands, and are significantly smaller than the 95 per cent Poisson noise on direct binned estimates at the same resolution (pink error bars). This follows from the fact that the particles in the original snapshot are now spread across multiple density bins, hence providing better statistics.

By dividing the total volume occupied by each halo into thin shells, we can also calculate the average radial velocities of the particles contained within the shells. These are shown for the low-resolution simulations in the panels below the density profiles in Figs [2]–[4]. These values will help us discuss below how well the assumption of equilibrium holds for each halo.

We will first discuss the behaviour of the dynamical profiles in the inner regions (around or even interior to the traditional convergence radius; Section [4.1]), then in the outer regions (around and beyond the virial radius; Section [4.2]).

4.1 Inner regions

The direct comparison of dynamical profiles (blue lines) with binned profiles from higher resolution simulations (black points) is of considerable interest: it addresses the question of whether our technique can partially correct for finite particle number in the innermost regions of the halo.

At radii below the approximate convergence radius of the low-resolution binned profiles ($r_{conv} = 3\epsilon$, indicated by the pink arrows in Figs [2]–[4]), our dynamical density cusps are steeper than the traditional binned profiles at the same resolution. This is particularly clear in the case of the Milky Way-mass haloes (Fig. [4]). Comparing our results to the binned distribution of the high-resolution simulations (black points), we see that the dynamical method is, in nearly all cases, able to predict the 'cuspier' behaviour of higher resolution simulations below r_{conv}. This is especially evident in the larger haloes due to the smaller Poisson noise in the central regions. Halo600 is an exception

---

[1]Using equation (14) in Ludlow, Schaye & Bower ([2019]) to calculate the convergence radius, with the constant κ_{P03} calibrated using a subset of our haloes at different resolutions, we obtained estimates between 2.6ϵ and 4.5ϵ across all snapshots. Our $r_{conv} = 3\epsilon$ estimate therefore falls within this range.
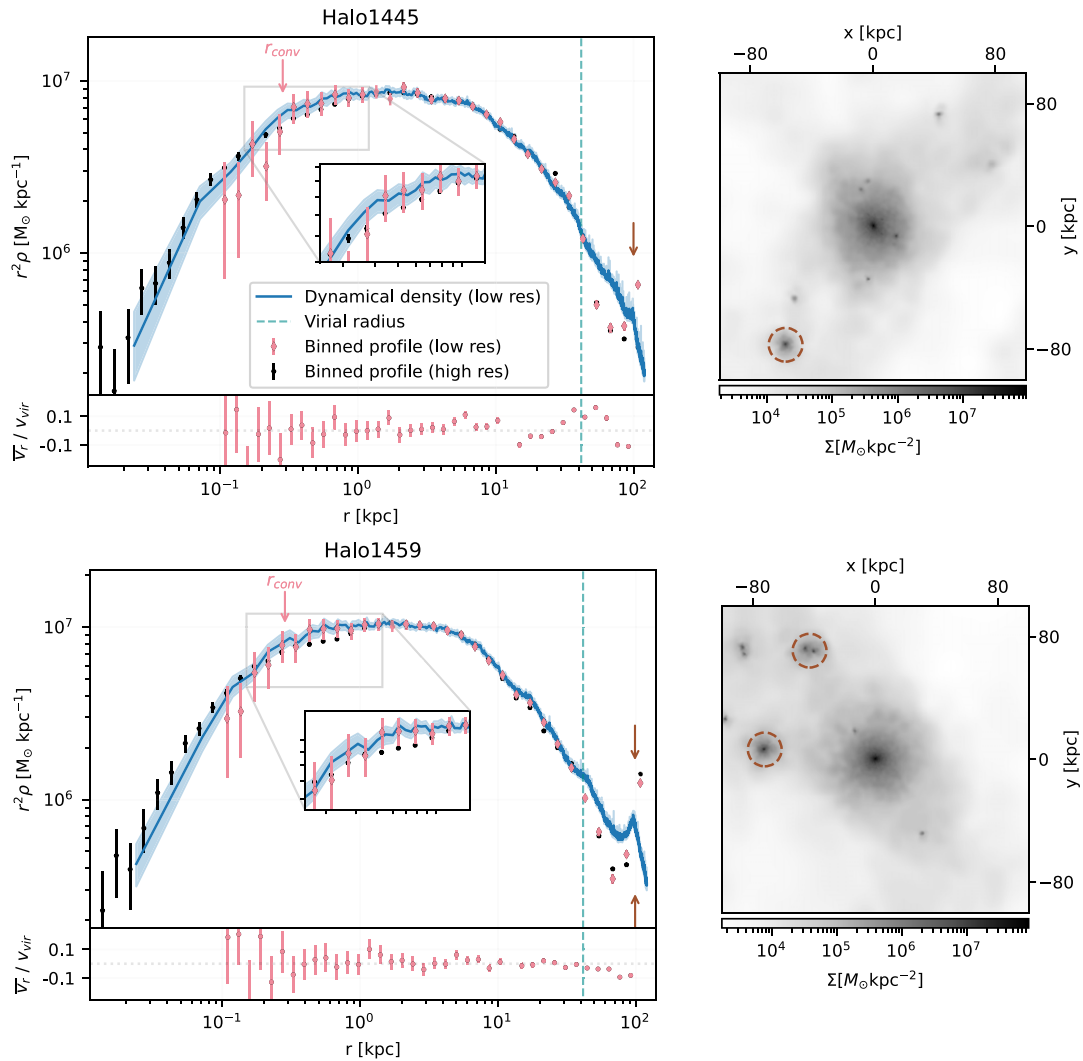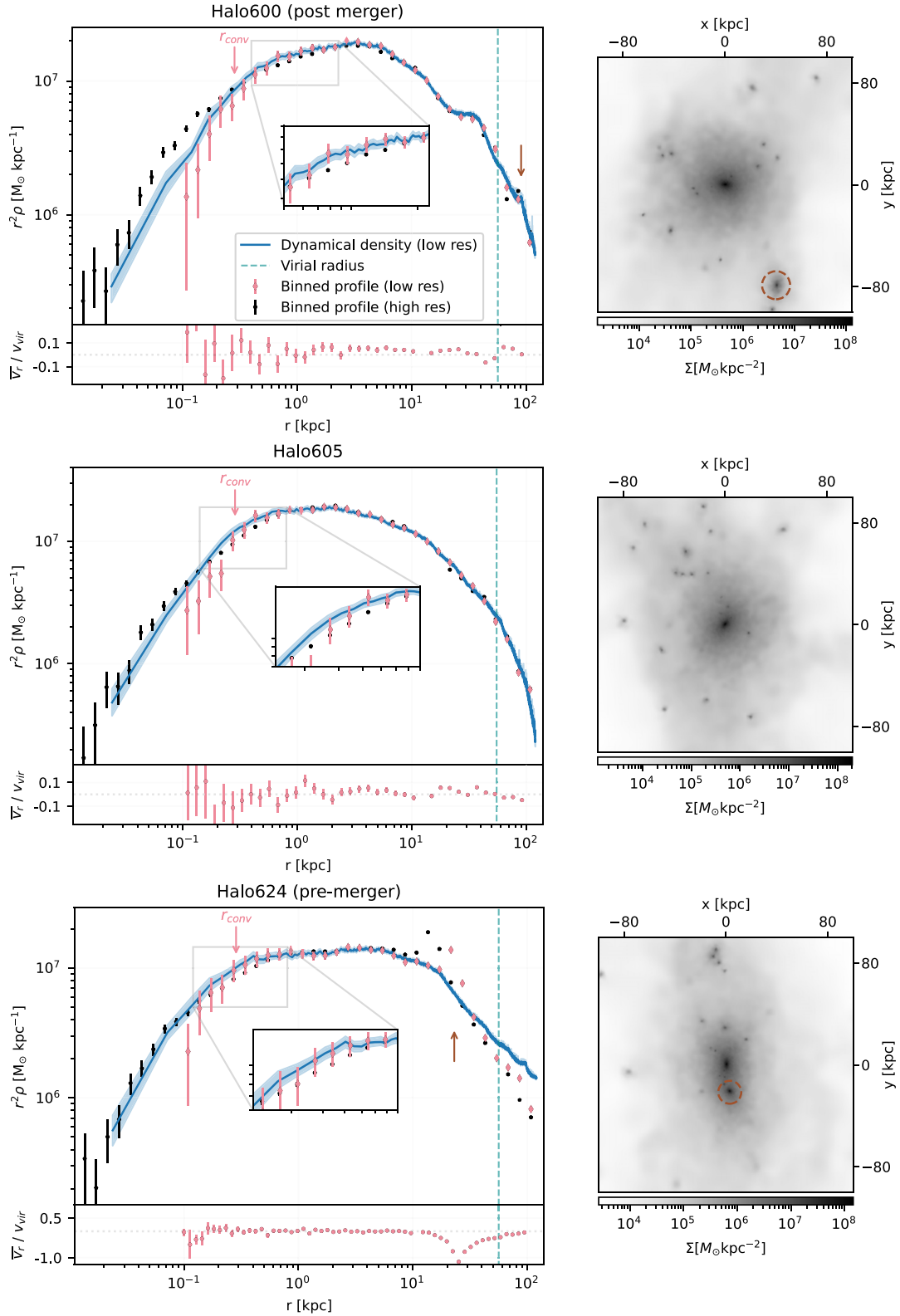
Figure 2. Density profiles multiplied by r^2 (left) and images of the dark matter density projected down the z-axis (right) for our two lowest mass dwarf haloes ($M \sim 2 \times 10^9 \, \mathrm{M_\odot}$). The dynamical density profiles obtained from the low-resolution snapshots agree very well with both the low- and high-resolution binned profiles for most of the radial extent of all the haloes. The largest variations between the dynamical and binned estimates are observed in the outer regions, beyond the virial radius, where large substructures in the outskirts cause spikes in the mass distribution. Any such substructures with mass greater than 3 per cent of the mass of the main halo are shown by dashed circles in the halo images, and by corresponding arrows in the dynamical profile plots. The panels below the density profiles show the variations in the average radial velocity of the particles contained within concentric shells as a fraction of the virial velocity, which can be used to quantify how close the low-resolution halo is to equilibrium. The arrows marked by r_{conv} indicate the radius corresponding to three times the value of the softening scale of the low-resolution simulations (i.e. r_{conv} for the low-resolution binned profiles).

in which the dynamically predicted density is substantially lower than that in the high-resolution simulation; Section 4.1.1 considers that case in some detail, and more broadly discusses caveats about making comparisons between low- and high-resolution simulations. None the less, in the other cases studied, the dynamically predicted cusp extends below r_{conv} of the low-resolution simulations, where very few particles are present at the time of the snapshot.[2] As well as being less biased than the binned profiles, our dynamical profiles also have lower numerical noise. On average across all haloes, the uncertainties at small radii (between ϵ and r_{conv}) are reduced by a factor of 12

compared to traditional binned estimates. Thus, our technique uses information about the entire phase space of the particles to produce more precise central density profiles that partially correct for the effects of softening and which are less subject to Poisson noise.

Poisson noise could also be mitigated by stacking binned profiles from adjacent snapshots (similarly to the procedure outlined in Vasiliev 2014). Fig. 5 shows an example of the binned profile obtained by stacking 6 adjacent snapshots of Halo1459. This is compared to our dynamical density profile (blue line) and to the binned profile obtained from a single snapshot at $z = 0$ (pink points). Stacking the profiles results in considerable reduction in shot noise, similar to the effect observed in the dynamical profile. However, the method fails to reproduce the steeper central gradient observed in the dynamical profile below the convergence radius, which implies a significant disagreement with the binned profile from the high-resolution runs. This is due to the fact that the stacked profile retains

---

[2]For the EDGE haloes, there are only 150–250 particles below r_{conv} and 350–450 for the VINTERGATAN-GM haloes; this is 0.38 and 0.007 per cent of the number of particles enclosed by the virial radius of the two simulation suites, respectively.

Figure 3. Same as Fig. 2 but for the three intermediate-mass dwarf haloes ($M \sim 5 \times 10^9 \, \mathrm{M_\odot}$). Similarly to the other cases, the dynamical density profiles from the low-resolution snapshots agree well with both binned profiles. Halo600 is an outlier since it recently had a merger close to the halo's centre that disrupted the equilibrium in the inner regions; as a result the plot of $\bar{v}_r/v_{\mathrm{vir}}$ shows significant deviations from zero at small radii. Halo624 has a large substructure within its virial radius that will reach the centre of the main halo and merge with it in the next $\sim$500 Myr. (The structure is found slightly closer to the centre in the high-resolution simulation.) The significant disruption caused by this substructure to the halo's equilibrium is also evident in the average radial velocity panel, but our dynamical method none the less recovers a sensible 'smoothed' density profile.
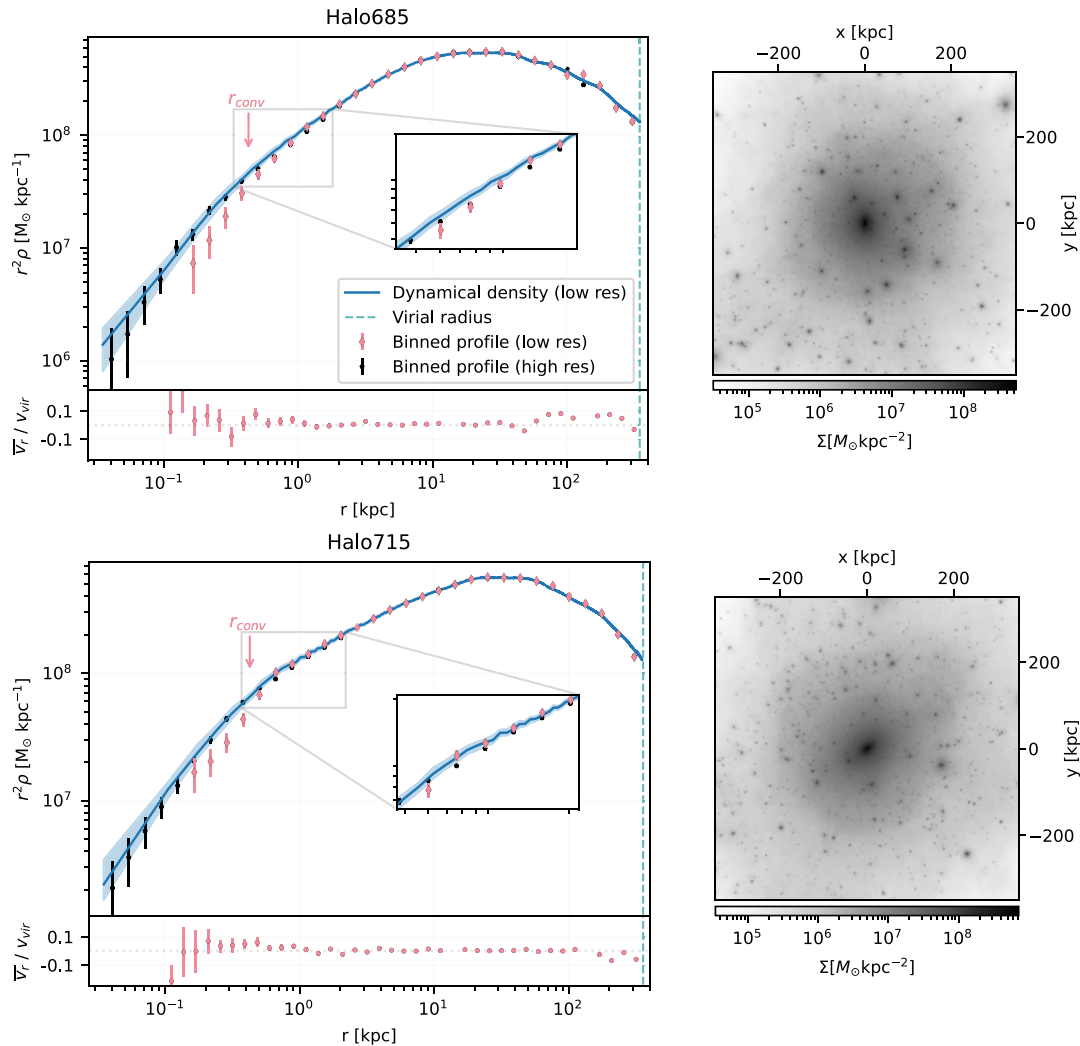
Figure 4. Same as Figs 2 and 3 but for the two most massive ($M \sim 10^{12}\,\mathrm{M_\odot}$) out of all seven haloes. Similarly to the other haloes, the dynamical density profiles from the low-resolution snapshots agree well with both the low- and high-resolution binned profiles. For efficiency, the dynamical profiles for these haloes were generated using only a randomly selected fraction (a third) of all the particles within the halo and therefore even smaller errors on the dynamical density profile are achievable in principle. In these examples, all substructures are small (less than 1 per cent of the halo mass) and do not have a visible effect on the density profiles.

the effects of gravitational softening and of relaxation caused by encounters between the particles in the low-resolution simulation as it evolves over time. By contrast, in the dynamical profile no softening is used and the orbits are integrated independently of each other, allowing the iteration process (Section 2.3) to correctly recover a steep central cusp. While in principle the stacked profile could also be iterated by combining it with our dynamical method, this would entail significant complexity due to the starting potentials in each snapshot differing from each other, as well as from the final combined potential. We therefore leave any investigation of such a combined stacked-dynamical profile to future work.

At radii just larger than r_{conv}, we notice a small but statistically significant density excess in both the binned and dynamical low-resolution profiles when compared with the high-resolution binned profiles. This excess only covers a few density bins and is more evident for some haloes (e.g. Halo605 and 624) than others; see the inset panels zoomed in on this radius in Fig. 3. Since this feature is also present when using binned methods, it must be unrelated to the inclusion of dynamical information into the calculations. We therefore leave investigation to a future study.

4.1.1 The challenge of direct comparisons between differing resolutions

Overall, the improvement offered by dynamical profiles over binned profiles is significant: the uncertainties at small radii are significantly mitigated compared to binned estimates, making it a substantially more precise technique. Qualitatively, it is clear that the dynamical profiles reproduce steeper profiles which appear to be in agreement with higher resolution simulations within the 95 per cent error bounds. However, quantifying how accurate the dynamical estimates are compared to the true density distributions (i.e. the density profiles that would be obtained from simulations of infinite resolution) is difficult for two reasons. The first is the problem of formulating a suitable comparison summary statistic; the second is the impact of small differences in halo formation and merger history on the final profile. We will describe each of these in turn.

The most natural way to measure the accuracy of a low-resolution density profile would be to construct a chi-squared test to decide whether the binned or dynamical profiles more accurately predict the high-resolution result. However, the size of the statistical errors on the
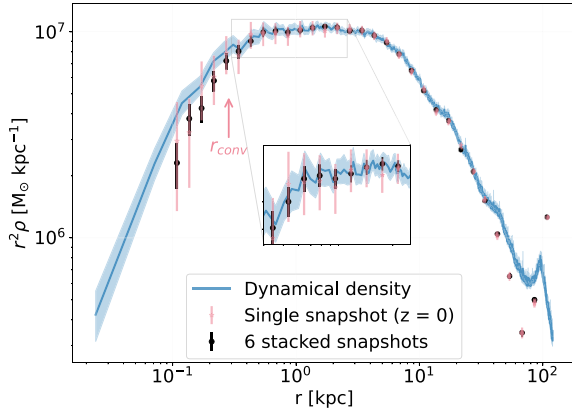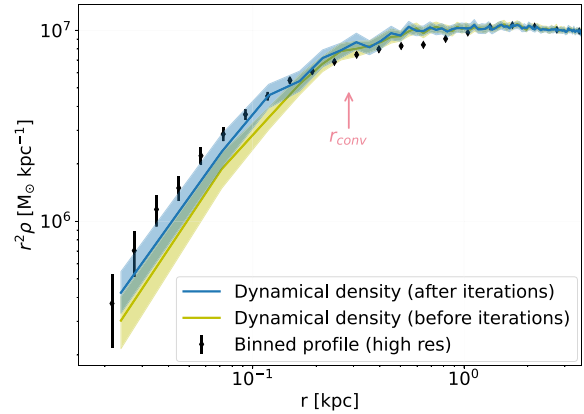
Figure 5. Binned density profile multiplied by r^2 obtained by stacking six consecutive snapshots from the low-resolution simulation of Halo1459. The dynamical density profile and the binned profile obtained from a single snapshot at $z = 0$ are also shown for comparison. Although Poisson noise is mitigated in the stacked profile, the method cannot correct the systematic softening and relaxation errors, and therefore underestimates central densities, unlike the dynamical profile.

Figure 6. Dynamical density profile multiplied by r^2 before and after the dynamical iteration process compared to the high-resolution binned profile, shown here for the example of Halo1459. The arrow marks the convergence radius of the low-resolution simulation binned profile (which, for clarity, is not itself shown). The effect of the iterations is especially evident at small radii, where they act to make the central regions moderately denser, in better agreement with the high-resolution profile.

dynamical profile are substantially smaller than those on the binned profile, putting the dynamical profiles at an automatic disadvantage in such a test. Even if one were to artificially inflate the dynamical profile error estimates, the results would remain very sensitive to the precise radial range over which the statistic is calculated. The dynamical profiles clearly predict more accurate densities interior to r_{conv}, but outside this radius the situation is more nuanced. In particular, at large radii, the dynamical profiles' tendency to wash out substructure would lead to a heavy χ^2 penalty (as will be discussed in Section 4.2). There is therefore no straightforward quantitative measurement of the improvement offered by dynamical density profiles, despite the clear qualitative advantages in the cusp region.

The second challenge relates to recent events in the formation and merger history, and is most clearly seen in the case of Halo600 (shown at the top of Fig. 3). As with the other examples, the gradient of the dynamical profile interior to r_{conv} is steeper than the low-resolution binned profile; however, unlike the other cases, the steepening in Halo600 is insufficient to reach agreement with the high-resolution binned profile. The reason can be traced to the halo's recent history in the respective simulations. The low-resolution version of Halo600 underwent a minor merger at $z = 0.03$ ($\sim$70 Myr before present day). This merger only occurred in the low-resolution version of the simulation. Although the mass of the merger is relatively small ($\sim 10^8$ M$_{\odot}$, around 2 per cent of the total host mass), its centre of mass before disruption is located within 1 kpc of the centre of mass of the main halo. By tracking the particles that formed the subhalo to $z = 0$, we find that they have traversed the halo from one side to the other, and remain in disequilibrium. The out-of-equilibrium behaviour is also visible as large fluctuations in the binned radial velocities as seen in the lower panel of the Halo600 plot in Fig. 3. Despite this, note that the dynamical density profile still performs somewhat better than the binned profile.

From the above analysis, we deduce that even a relatively small merger might affect the equilibrium of a halo. A statistical study on a larger sample of haloes is necessary to constrain the exact relationship between merger-to-main halo mass ratio and the effect that the merger events have on the dynamical profile. Other features will also play a role, such as the object infall velocity or the angle

of collision. The investigation of these effects is beyond the scope of this work.

### 4.1.2 Effect of potential iterations

Having established that dynamical profiles offer an accuracy improvement over binned profiles near the centres of haloes, albeit one that is hard to quantify, we now consider the effect of the iterative part of our algorithm (Section 2.3) in achieving this.

Fig. 6 shows the effect that the iteration process outlined has on the dynamical profile. After the iterations, the profile's central gradient becomes moderately steeper. This can be understood by considering that the particles previously located at larger radii are now allowed to extend further inwards compared to their original positions in the snapshot, hence increasing the density in the inner regions. Note that the increase in central density may appear to violate mass conservation, since the total mass of the halo should be unaltered. However, we verified that the mass enclosed converges to the same value at the virial radius; the volume of the sphere inside r_{conv} is just 3×10^{-5} per cent of the total volume inside the virial radius, and therefore a very small reduction in density across a large range of radii is able to provide the mass for an increased density cusp.

Overall, we therefore conclude that the iterative component of the algorithm is important not just for self-consistency (as argued in Section 2.3) but also to achieve the increased densities interior to the binned profile's convergence radius. Given that we kept actions fixed (to first order) during the iterations, one can envisage them as adiabatically transforming away some numerical effects of softening.

4.1.3 Comparison at ultra-high resolution

So far, we have applied our dynamical method to the *low*-resolution snapshots and compared our results against the binned profiles obtained from the *high*-resolution versions of the simulations. In order to understand whether this improvement is independent of resolution, we now test the dynamical approach on the *high*-resolution simulations and compare the results to *ultra-high*-resolution snapshots.
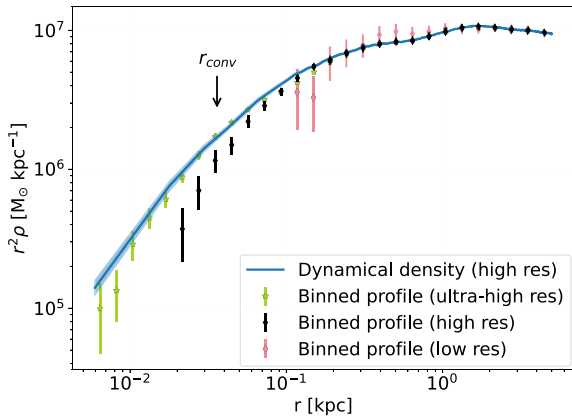
Figure 7. Dynamical density profile multiplied by r^2 obtained from the *high*-resolution simulation of Halo1459, compared to the binned density profiles of the high and ultra-high resolution snapshots. The binned profile obtained from the low-resolution snapshot is shown for reference. The arrow indicates the approximate convergence radius of the high-resolution binned profile (3ϵ). The dynamical density profile from the high-resolution simulation predicts the ultra-high-resolution simulation well, underscoring how the method can be applied at any resolution to extract additional information.

Fig. 7 shows the dynamical density profile calculated from the high-resolution simulation of Halo1459 compared to the binned distribution from an ultra-high-resolution simulation with $\epsilon \simeq 6$ pc (half the softening length of the high-resolution snapshots previously analysed). We take Halo1459 as an example, but similar results are observed for the other haloes.

All the conclusions drawn in the case of the low-resolution dynamical profile are still valid when the code is applied to the high-resolution snapshot: the dynamical density shows smaller uncertainties, a steeper cusp that extends further inwards and approximately follows the higher resolution binned profile, and a small density excess at $r \sim r_{\mathrm{conv}}$ in the lower resolution profile. Overall, this confirms that the improvements obtained by adding dynamical information to the profiles continue even for increasingly precise simulations, making them resolution-independent.

In Fig. 8, we show the dynamical profile obtained from the high-resolution simulation of Halo600. When the dynamical code was previously applied to the low-resolution simulation (top of Fig. 3), we saw that the steepening in the cusp was insufficient to reach agreement with the high-resolution binned profile. This is not the case when the dynamical profile is calculated from the high-resolution snapshot: the cusp of the dynamical profile is entirely consistent with the ultra-high-resolution binned profile. This provides further evidence that the disagreement between the dynamical and binned profiles at small radii in the low-resolution case is a result of the disequilibrium caused by the merger event, which did not occur in the high-resolution version.

4.2 Outer regions

Having shown that the dynamical profile technique performs well in suppressing numerical noise at small radii (comparable to the convergence radius), we next consider its predictions at large radii (comparable to the virial radius r_{vir}). At such large radii, finite particle number is unlikely to be a limiting factor in drawing physical conclusions and therefore the motivation for studying the dynamical profile is different. Specifically, we are interested in understanding the degree to which haloes may be considered equilibrium structures;
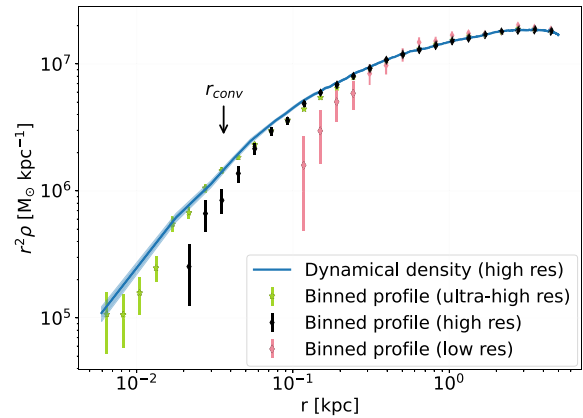
Figure 8. Same as Fig. 7 but for Halo600. The dynamical profile from the high-resolution simulation of this halo shows a steep cusp consistent with the ultra-high-resolution binned profile. The high-resolution simulation, unlike the low-resolution version, did not recently undergo a merger close to the halo's centre. This provides further evidence that the disagreement between the dynamical and binned profiles seen at small radii in the low-resolution case is due to disequilibrium caused by the merger event.

departure from such equilibrium invalidates our assumptions and therefore should lead to an inaccurate profile. The virial radius roughly defines the point past which most particles are no longer gravitationally bound to the halo, such that infalling particles from the halo's environment begin to dominate.

We are able to study the dynamical profiles beyond r_{vir} for dwarf-scale haloes, since the zoom region extends several times further out. Beyond the virial radius we find, as expected, that the dynamical profiles are typically inaccurate; see Halo1445 and 1459 in Fig. 2 for particularly clear cases.

This provides one clear signature of out-of-equilibrium dynamics. However, another way to measure departures from equilibrium is via the binned average radial velocities of the particles ($\bar{v}_r$), which should be consistent with zero in equilibrium. Measured values of $\bar{v}_r$ are shown in the panels below the density profiles in Figs 2–4. As expected, these values deviate strongly from zero outside the virial radius, confirming our interpretation above. However, more surprisingly, the mean velocity values deviate from zero even *interior* to the virial radius, in regions where the binned and dynamical profiles fully agree (e.g. in Halo600, 605, 1459 over the radial range 1 kpc $< r <$ 40 kpc). The root-mean-square deviation of the radial velocities of all haloes (excluding Halo624) in the region $r < r_{\mathrm{vir}}$ is of order ~ 5 per cent of the virial velocity. These deviations are statistically important, and yet do not appear to have a significant effect on the overall density structure that is in good agreement with the binned estimates. This suggests that the dynamical profiles are robust to even significant violations of their equilibrium assumption.

4.2.1 The role of substructures

Although dynamical profiles remain robust despite the existence of smooth inflows detectable well interior to the virial radius, a more difficult challenge is posed by substructures. Most haloes have spikes in the *binned* density distribution at certain radii: for Halo600, 1445, and 1459 (Fig. 2, and top of Fig. 3) these can be seen beyond the virial radius at $r \sim 90$–100 kpc, while for Halo624 (bottom of Fig. 3) we see them much closer to the centre at $r \sim 10$–20 kpc. We refer to the locations of these features as r_{spike}. We verified that these local density spikes are indeed caused by substructures (see brown

circles in the haloes density images in Figs 2–4), which each contain between 3 and 9 per cent of the mass of the main halo. All the other substructures present within the reflecting boundary have masses below 0.5 per cent of the main halo's mass.

The dynamical density profile does not reproduce spikes associated with substructure; by design, it smears them out along their orbit without taking into account the self-binding of the substructure. This leads to systematic differences between the binned and dynamical profiles, since the spike is smoothed out while conserving the total mass. This effect is especially evident outside the virial radius in Halo1445 and 1459 (Fig. 2). In these cases, substructures (indicated by brown arrows at the appropriate radii on the density plots) coincide with significant disagreements between binned and dynamical halo profiles.

Halo624 contains a large substructure of mass $\sim 1.4 \times 10^9\,\mathrm{M_\odot}$ within its virial radius (at $r \sim 20$–25 kpc). This is clearly visible in the density image at the bottom of Fig. 3. The substructure will reach the centre of the main halo and merge in the next ~ 500 Myr (based on its estimated infall velocity at $z = 0$), and the disruption to the halo's equilibrium caused by the presence of substructure is also evident in the large deviations from zero in the average radial velocity panel. Despite this, the dynamical profile still faithfully represents the density distribution at radii between the centre of the halo and the location of the substructure. This shows that the effects of the dark matter spike are localized to the area around the substructure, and our method can represent the correct density distribution in other regions of the halo.

Halo605 provides an example with no large substructures present within the entire volume analysed. Despite fluctuations of the binned mean velocity, the dynamical profile agrees with the binned profile up to radii of 100 kpc which is around $2r_{\mathrm{vir}}$. Taken with the discussion above, this counterexample strongly suggests that substructures, rather than smooth radial flows, are the dominant factor in determining whether binned and dynamical profiles differ significantly, and that the effect of substructures on the profile is always localized.

4.2.2 Effect of the reflecting boundary

As described in Section 2.1, the dynamical density profile requires an outer boundary condition. We have assumed a perfectly reflecting wall, which is equivalent to assuming that the particles flowing inwards across the boundary are exactly balanced by the flux outwards, in keeping with our broader assumption of dynamical equilibrium. However, there remains the freedom to move the reflecting wall to an arbitrary location. We carried out a number of experiments to determine the effect of this choice. If, for example, a boundary is placed inside the virial radius we found that the dynamical density profile is insensitive to the particular choice of location. However, in order to probe the outer parts of the halo the results above were all presented with the boundary outside the virial radius. In this case, there is more sensitivity to the particular choice of location.

An example is shown in Fig. 9 for Halo605. As usual, the binned profile is shown by pink points with error bars while dynamical profiles are represented as lines. Here, however, we show two alternative dynamical profiles: one with the reflecting boundary moved inwards to 100 kpc ($\simeq 2$ times the virial radius, as previously adopted, and illustrated here with a blue line) and one with the reflecting boundary moved outwards to 200 kpc ($\simeq 4$ times the virial radius, illustrated with a grey line). This shift causes the dynamical
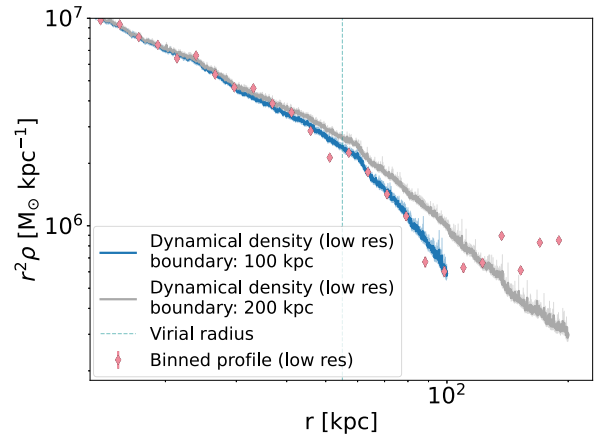
Figure 9. Zoom into the outer regions of the dynamical profile of Halo605 (middle of Fig. 3) when the reflecting boundary is placed at 100 kpc and then moved to 200 kpc compared to the low-resolution binned profile. The dynamical profile agrees well with the binned one when the boundary is placed anywhere up to 100 kpc, around twice the virial radius, but differs once contributions from particles out to 200 kpc are included in the calculations. These discrepancies propagate inwards to smaller radii, even below the virial radius (55 kpc, indicated by the vertical dashed line). This behaviour reflects our algorithm's extrapolation of how particles and substructures in the outskirts, while currently unbound, will ultimately fall into the halo at later times in the simulation, altering the density distribution.

profile to deviate from the binned density in the range $r_{\mathrm{vir}} < r < 2r_{\mathrm{vir}}$, where there was previously agreement.

The change is caused by particles that, at the time of the snapshot, are exterior to $2r_{\mathrm{vir}}$ but infalling, such that they spread to lower radii when the equilibrium assumption is imposed. The binned profile shows a 'kink' at $\simeq 100$ kpc, which means that, in this particular case, there is a relatively large mass in such infalling particles. When the reflecting wall is located at $2r_{\mathrm{vir}}$, these particles are safely isolated outside of the boundary, and therefore cannot affect the density profile.

In a sense, moving the reflecting wall to increasingly large radii provides a prediction of the future profile, since it extrapolates to a time when far-out particles have been able to fall into the inner regions. However, we did not study to what extent this can actually be used to make meaningful predictions and we caution that the actual process via which infalling particles relax into virial equilibrium is unlikely to be fully captured; in effect, our algorithm assumes conservation of their adiabatic invariants which is unlikely to be correct in detail.

For practical purposes, the most conservative choice of reflecting wall boundary is at the virial radius, but our results show that it is entirely possible to obtain accurate profiles out to twice the virial radius. Beyond this, dynamical profiles with extended radial range may be of interest for understanding the accretion processes of haloes and 'splashback' features (Adhikari, Dalal & Chamberlain 2014; Diemer & Kravtsov 2014; More, Diemer & Kravtsov 2015; Lucie-Smith et al. 2022; Shin & Diemer 2023), something we will investigate in the future.

5 CONCLUSIONS AND DISCUSSION

We presented a new method to estimate spherically averaged densities in cosmological dark matter haloes. Instead of binning the particle in a snapshot by radius, which is the most obvious and prevalent approach, we use the velocity information in the snapshot

to 'smear' each particle along a trajectory, substantially reducing Poisson noise. Such a method has been proposed before (Read & Gilmore 2005; Pontzen & Governato 2013), but our work is the first systematic investigation of the approach. Additionally, we derive new corrections to take into account the integrable singularities at apocentre and pericentre, and introduce an iterative process to obtain a self-consistent potential–density pair. After iteration, we obtain central density estimates that (except in one case, Halo600, where a recent merger has occurred) follow the trend set by higher resolution simulations. The agreement persists interior to the binned profile convergence radius, and all the way down to the simulation softening length. This highlights how our technique can squeeze extra information about the central regions of haloes from existing simulations.

In the outer regions, the dynamical profiles continue to agree with the binned profiles even out to several times the virial radius, provided that no substructures are present. If substructures are present, the assumption of equilibrium is locally broken and the profiles in the vicinity of the substructure are 'smoothed' relative to the binned profiles. None the less, the overall profiles remain accurate. Eventually, at approximately $r \sim 4r_{\rm vir}$, effects from the haloes' environments start to dominate, bringing the haloes too far out of equilibrium for the dynamical profiles to give meaningful density estimates. Including particles from these distant halo outskirts can produce changes to the dynamical profiles, sometimes even at radii below the virial radius. This is not a surprising result since the particles at large radii will eventually fall into the halo at future times in the simulation, and the dynamical approach is extrapolating the orbits of these particles accordingly. However, whether the resulting profile can be considered a 'prediction' of the growth of the dark matter distribution at later times remains to be investigated.

These effects in the outer parts of the halo relate to the departure from perfect equilibrium (or phase mixing), which is one of two key assumptions underlying the method. The second assumption is that the potential is spherically symmetric; this assumption is, in fact, broken by all our simulated haloes, since they have triaxial equipotential surfaces. The fact that the dynamical profiles are accurate despite this broken assumption warrants further discussion.

Orkney et al. (2023) estimated the shapes of the five least massive dark matter haloes studied in this work by calculating the intermediate-to-major and minor-to-major axial ratios (b/a and c/a) up to approximately 20 kpc in radius. The exact shape of each halo is not constant with radius: the c/a ratio for all the haloes varies within the interval 0.4–0.8 (ratios of exactly 1 indicate perfect sphericity). The DMO haloes are generally the least spherical near their centre, becoming increasingly more spheroidal at radii beyond the cusp ($\gtrsim 1$ kpc). Nevertheless, the dynamical density profiles are able to correctly represent the density distributions for the entire radial extent of the haloes.

The nature of the particles' orbits in an aspherical system is very different from the orbits that would be observed in a spherically averaged version of the same potential. In the spherical case, the angular momentum of individual particles is always constant; this is not the case in aspherical systems where only the total angular momentum of the entire system is conserved. This allows specific types of orbits (which would not be allowed in a spherical potential) to exist, such as box orbits that plunge through the centre of the halo. Therefore, the fact that we are able to infer reliable results about the haloes' properties using only an artificial version of the dynamics that does not correspond to the real trajectories of the particles is not a straightforward outcome.

However, such an outcome was previously predicted by relying on having a distribution function of particles in equilibrium (Pontzen et al. 2015). For every particle that is on an orbit losing angular momentum, there must be another particle on an orbit gaining angular momentum. To put it another way, the net flux of particles through the spherical action space must be everywhere zero, and so in a statistical sense, averaged across all particles, the spherical orbits remain a good approximation. For a more technical discussion, see Pontzen et al. (2015). This work provides additional evidence that this mapping from a real triaxial system on to an effective spherical system is able to give accurate insights into dark matter halo structure. That said, the dynamical density method could be readily extended beyond the assumption of spherical symmetry, similarly to other mass modelling techniques (Schwarzschild 1979; Syer & Tremaine 1996).

Overall, our dynamical method for the evaluation of dark matter density profiles is a powerful tool that can represent the correct mass distribution even when its fundamental assumptions are partially broken, making it largely applicable to a wide range of systems.

However, dark matter haloes in the real Universe have potentially been altered by baryonic effects, something that we have not investigated at all in this paper. In forthcoming work, we will apply our dynamical density code to hydrodynamical simulations. Adding baryons to the simulations will likely alter the shape of the profile's inner regions, transforming the cusp into a flatter core. At a technical level, the gravitational potential can no longer be made fully self-consistent with the dark matter density distribution, and the potential will need to be evaluated directly from the snapshot for the baryonic component. The iterative procedure that we have outlined will therefore need to be refined before we can use it in such cases.

ACKNOWLEDGEMENTS

DATA AVAILABILITY

Data are available upon reasonable request. The code used to calculate the dynamical density profiles is publicly available on GitHub (repository: dynamical_density_profiles).

REFERENCES

Adhikari S., Dalal N., Chamberlain R. T., 2014, J. Cosmol. Astropart. Phys., 2014, 019
Agertz O. et al., 2019, MNRAS, 491, 1656

Allgood B., Flores R. A., Primack J. R., Kravtsov A. V., Wechsler R. H., Faltenbacher A., Bullock J. S., 2006, MNRAS, 367, 1781

Angulo R. E., Hahn O., 2022, Living Rev. Comput. Astrophys., 8 1

Battaglia G., Helmi A., Tolstoy E., Irwin M., Hill V., Jablonka P., 2008, ApJ, 681, L13

Burkert A., 1995, ApJ, 447, L25

Callingham T. M., Cautun M., Deason A. J., Frenk C. S., Grand R. J. J., Marinacci F., Pakmor R., 2020, MNRAS, 495, 12

Chemin L., de Blok W. J. G., Mamon G. A., 2011, AJ, 142, 109

de Blok W. J. G., McGaugh S. S., Rubin V. C., 2001, AJ, 122, 2396

Dehnen W., Read J. I., 2011, Eur. Phys. J. Plus, 126, 55

De Leo M., Read J. I., Noel N. E. D., Erkal D., Massana P., Carrera R., 2023, preprint (arXiv:2303.08838)

Diemand J., Moore B., Stadel J., 2004, MNRAS, 353, 624

Diemer B., 2022a, MNRAS, 513, 573

Diemer B., 2022b, MNRAS, 519, 3292

Diemer B., Kravtsov A. V., 2014, ApJ, 789, 1

Dubinski J., Carlberg R. G., 1991, ApJ, 378, 496

Dutton A. A., Macciò A. V., 2014, MNRAS, 441, 3359

Einasto J., 1965, Trudy Astrofizicheskogo Instituta Alma-Ata, 5, 87

El-Zant A., Shlosman I., Hoffman Y., 2001, ApJ, 560, 636

Fielder C. E., Mao Y.-Y., Zentner A. R., Newman J. A., Wu H.-Y., Wechsler R. H., 2020, MNRAS, 499, 2426

Flores R. A., Primack J. R., 1994, ApJ, 427, L1

Frenk C., White S., 2012, Annalen der Physik, 524, 507

Frenk C. S., White S. D. M., Davis M., Efstathiou G., 1988, ApJ, 327, 507

Fukushige T., Makino J., 2001, ApJ, 557, 533

Gao L., Navarro J. F., Frenk C. S., Jenkins A., Springel V., White S. D. M., 2012, MNRAS, 425, 2169

Genina A. et al., 2017, MNRAS, 474, 1398

Ghigna S., Moore B., Governato F., Lake G., Quinn T., Stadel J., 2000, ApJ, 544, 616

Hague P. R., Wilkinson M. I., 2013, MNRAS, 433, 2314

Hayashi K., Chiba M., Ishiyama T., 2020, ApJ, 904, 45

Hernquist L., 1990, ApJ, 356, 359

Jing Y. P., Suto Y., 2002, ApJ, 574, 538

Lucie-Smith L., Peiris H. V., Pontzen A., Nord B., Thiyagalingam J., Piras D., 2022, Phys. Rev. D, 105, 103533

Ludlow A. D., Schaye J., Bower R., 2019, MNRAS, 488, 3663

Marchesini D., D'Onghia E., Chincarini G., Firmani C., Conconi P., Molinari E., Zacchei A., 2002, ApJ, 575, 801

More S., Diemer B., Kravtsov A. V., 2015, ApJ, 810, 36

Navarro J. F., Eke V. R., Frenk C. S., 1996a, MNRAS, 283, L72

Navarro J. F., Frenk C. S., White S. D. M., 1996b, ApJ, 462, 563

Navarro J. F., Frenk C. S., White S. D. M., 1997, ApJ, 490, 493

Navarro J. F. et al., 2004, MNRAS, 349, 1039

Nipoti C., Binney J., 2014, MNRAS, 446, 1820

Oh S.-H. et al., 2015, AJ, 149, 180

Oldham L. J., Auger M. W., 2016, MNRAS, 457, 421

Oman K. A., Marasco A., Navarro J. F., Frenk C. S., Schaye J., Bení tez-Llambay A., 2018, MNRAS, 482, 821

Orkney M. D. A. et al., 2021, MNRAS, 504, 3509

Orkney M. D. A. et al., 2022, MNRAS, 515, 185

Orkney M. D. A., Taylor E., Read J. I., Rey M. P., Pontzen A., Agertz O., Kim S. Y., Delorme M., 2023, MNRAS, 525, 3516

Pineda J. C. B., Hayward C. C., Springel V., Mendes de Oliveira C., 2016, MNRAS, 466, 63

Planck Collaboration XVI, 2014, A&A, 571, A16

Planck Collaboration XIII, 2016, A&A, 594, A13

Pontzen A., Governato F., 2012, MNRAS, 421, 3464

Pontzen A., Governato F., 2013, MNRAS, 430, 121

Pontzen A., Roškar R., Stinson G., Woods R., 2013, Astrophysics Source Code Library, record ascl:1305.002

Pontzen A., Read J. I., Teyssier R., Governato F., Gualandris A., Roth N., Devriendt J., 2015, MNRAS, 451, 1366

Popolo A. D., Pace F., 2016, Ap&SS, 361, 162

Power C., Navarro J. F., Jenkins A., Frenk C. S., White S. D. M., Springel V., Stadel J., Quinn T., 2003, MNRAS, 338, 14

Read J. I., Gilmore G., 2005, MNRAS, 356, 107

Read J. I., Agertz O., Collins M. L. M., 2016, MNRAS, 459, 2573

Read J. I., Iorio G., Agertz O., Fraternali F., 2017, MNRAS, 467, 2019

Read J. I., Walker M. G., Steger P., 2019, MNRAS, 484, 1401

Rey M. P., Starkenburg T. K., 2021, MNRAS, 510, 4208

Rey M. P., Pontzen A., Agertz O., Orkney M. D. A., Read J. I., Saintonge A., Pedersen C., 2019, ApJ, 886, L3

Rey M. P., Pontzen A., Agertz O., Orkney M. D. A., Read J. I., Rosdahl J., 2020, MNRAS, 497, 1508

Salucci P., Lapi A., Tonini C., Gentile G., Yegorova I., Klein U., 2007, MNRAS, 378, 41

Schwarzschild M., 1979, ApJ, 232, 236

Shin T., Diemer B., 2023, MNRAS, 521, 5570

Shin T. et al., 2019, MNRAS, 487, 2900

Syer D., Tremaine S., 1996, MNRAS, 282, 223

Teyssier R., 2002, A&A, 385, 337

Vasiliev E., 2014, MNRAS, 446, 3150

Vogelsberger M., Marinacci F., Torrey P., Puchwein E., 2020, Nat. Rev. Phys., 2, 42

Walker M. G., Peñarrubia J., 2011, ApJ, 742, 20

Wang J., Bose S., Frenk C. S., Gao L., Jenkins A., Springel V., White S. D. M., 2020, Nature, 585, 39

Zhao H., 1996, MNRAS, 278, 488

Zoutendijk S. L., Brinchmann J., Bouché N. F., den Brok M., Krajnović D., Kuijken K., Maseda M. V., Schaye J., 2021, A&A, 651, A80

This paper has been typeset from a TeX/LaTeX file prepared by the author.